

CrossMark  
click for updatesCite this: *Soft Matter*, 2014, 10, 9413

## “Crystal-clear” liquid–liquid transition in a tetrahedral fluid

Francis W. Starr<sup>a</sup> and Francesco Sciortino<sup>b</sup>

For a model known to exhibit liquid–liquid transitions, we examine how varying the bond orientational flexibility affects the stability of the liquid–liquid transition relative to that of the crystal phases. For very rigidly oriented bonds, the crystal is favored over all amorphous phase transitions. We find that increasing the bond flexibility decreases both the critical temperature  $T_c$  for liquid–liquid phase separation and the melting temperature  $T_m$ . The effect of increasing flexibility is much stronger for melting, so that the distance between  $T_c$  and  $T_m$  progressively reduces and inverts sign. Under these conditions, a “naked” liquid–liquid critical point bulges out in the liquid phase and becomes accessible, without the possibility of crystallization. These results confirm that a crystal-clear, liquid–liquid transition can occur as a genuine, thermodynamically stable phenomenon for tetrahedral coordinated particles with flexible bond orientation, but that such a transition is hidden by crystallization when bonds are highly directional.

Received 18th August 2014  
Accepted 23rd September 2014

DOI: 10.1039/c4sm01835d

www.rsc.org/softmatter

### 1. Introduction

Molecules or particles with a dominant tetrahedral bonding geometry are characterized by liquids in which substantial empty spaces exist. The local coordination, around four, is significantly smaller than the typical coordination of simple atomic fluids, where about twelve neighbors surround each atom, and consequently the packing fraction of tetrahedral fluids is typically  $\approx 40\%$  smaller. Similarly, the ordered phases of tetrahedral particles are characterized by open crystals in which all four bonds are formed. As in the liquid state, the crystal density is significantly lower (by around a factor of two or more) than the body-centered (BCC) or face-centered (FCC) crystal structures of typical atomic systems. In nature, water and silicon are examples of substances in which empty liquid states originate from the directionality of the tetrahedral inter-particle interactions, and for which the open diamond structure (respectively formed by the oxygen or silicon atoms) is the stable crystal phase at ambient pressure.

It has been argued that the existence of empty spaces in tetrahedral liquids opens the possibility of a liquid–liquid (LL) phase transition in a pure, single-component system.<sup>1</sup> The possibility of LL phase transition in a pure substance was first proposed for water,<sup>2</sup> and later-on extended to interpret the behavior of several other atomic and molecular network forming systems.<sup>3–5</sup> A LL transition has been directly observed in phosphorus<sup>6</sup> and cerium.<sup>7</sup> For network fluids, the LL transition

is characterized by the emergence, at low temperature, of liquid states with two distinct structures, differing in their local density, which drives phase separation; the two liquids are commonly referred to as low-density liquid (LDL) and high-density (HDL) liquid. There have been many attempts to understand the underlying interactions required to realize such a transition. For the case of isotropic particle interactions, the presence of two distinct length and energy scales in the inter-particle potential can theoretically give rise to a LL transition.<sup>8,9</sup> In contrast, for the case of tetrahedral directional interactions, the symmetry between the structure of occupied and empty space readily theoretically allows repeated network structures.<sup>1,10,11</sup> More specifically, the low density phase consists of a single network of tetrahedrally coordinated particles, while the high density phase is characterized by partial interpenetration of two local tetrahedral networks (*i.e.* a second local tetrahedral network occupying the unoccupied space of the first network). Under these conditions, two distinct second-order critical points (gas–liquid and liquid–liquid) are present in the phase diagram of the system. Directionality can also arise in binary systems with isotropic interactions, such as silica, due to size asymmetry and electrostatics.<sup>12</sup>

The interpenetration mechanism that leads to a liquid–liquid transition has been numerically investigated in detail for DNA-functionalized nanoparticles, a colloidal analog of tetrahedral molecules.<sup>1,11,13,14</sup> Indeed, a variety of techniques to create colloids or nanoparticles with customizable interactions have been developed over the past 20 years.<sup>15,16</sup> These ‘designer atoms’ can potentially control both the number of links, or valence, as well as the bonding distance, relative to the core size. As a consequence, the phase behavior of these systems can include a number of interesting features, including ‘empty

<sup>a</sup>Department of Physics, Wesleyan University, Middletown, Connecticut 06459, USA. E-mail: [fstarr@wesleyan.edu](mailto:fstarr@wesleyan.edu)

<sup>b</sup>Dipartimento di Fisica, Università di Roma La Sapienza, Piazzale Aldo Moro 2, I-00185 Roma, Italy. E-mail: [francesco.sciortino@uniroma1.it](mailto:francesco.sciortino@uniroma1.it)

liquids',<sup>17,18</sup> micellar and other cluster phases.<sup>19,20</sup> In particular, the possibility of thermodynamically distinct amorphous states from a single component system has garnered much attention, since – as we have alluded to above – it may help to explain the unusual behavior of important natural liquids, like water and silica. Of the various approaches for creating designer atoms, tethering of DNA to the nanoparticle (NP) core is particularly attractive, as the bonding specificity and relative rigidity of double-stranded (ds) DNA allow for 'lock-and-key' linkages with a highly variable range.<sup>21–24</sup>

For the case of small NP units decorated with DNA with tetrahedral symmetry, we have previously developed a coarse-grained molecular model to investigate their phase behavior and structure, and their assembly into large-scale amorphous networks.<sup>13,25–27</sup> In this case, four single-stranded (ss) palindromic DNA strands are attached to a small core NP to provide a clean model for tetrahedral particles with limited valence. Network assembly occurs by the hybridization of dsDNA to connect NP. Due to base pair selectivity, each strand can participate in only one dsDNA 'bond' with a neighboring NP, eliminating possible complications of multiple or shared bonding situations. Distinct from atomic systems, these particles can interpenetrate without significant energy costs due to the small core size relative to the DNA length, emphasizing the role of the empty space in the bonded network. Fig. 1 shows an example of the model particles and their ability to interpenetrate at high density. The resulting model incorporates a high degree of tetrahedrality by design, and displays clear liquid–liquid transitions associated with the interpenetration of locally distinct networks.<sup>1,11</sup>

Previous studies on the liquid–liquid transition generally either found that the critical point is metastable with respect to the crystal phase, as expected for water,<sup>2,28–31</sup> or did not evaluate the relative stability of the liquid and crystal states. The importance of this non-equilibrium condition to the LL transition and of the finite lifetime of the liquid state has mostly escaped discussion. Only recently have such topics come into play,<sup>32–38</sup> and a number of studies have examined the possible interference between the liquid–liquid transition and crystallization. To understand this interference, one must consider how the intermolecular interactions differently affect crystal formation and the LL transition. In the case of crystallization, the

quest for a self-assembled photonic colloidal diamond crystal<sup>39</sup> has stimulated the investigation of the mechanisms underlying crystallization in tetrahedral crystals.<sup>40,41</sup> Simple models where the bond orientational flexibility can be varied have shown that crystallization of open structures (the equivalent of hexagonal and cubic ice) is strongly favored by directional bonds.<sup>40</sup> Furthermore, it has been discovered that very flexible bonds destabilize the open crystal structure so much that the liquid phase may remain thermodynamically stable (lower free energy than the crystal) down to zero temperature for a wide region of densities.<sup>42–44</sup> Networks of DNA tetravalent particles possibly provide an example of highly flexible particles that never crystallize.<sup>45</sup> The impact of flexibility on the LL transition is comparatively less well studied.

The role of the orientational bond flexibility in the liquid–liquid transition has been recently investigated in an ideal model of colloidal tetrahedral molecules,<sup>46</sup> and these results suggest that bond flexibility affects crystallization and the liquid–liquid transition differently. For highly directional bonds, crystallization is dominant and the liquid–liquid transition is deeply metastable (if not pre-empted by the spontaneous formation of crystal seeds). On increasing the bond flexibility, the liquid–liquid critical temperature approaches the crystallization temperature and then 'pops-up' above the melting temperature as a thermodynamically stable phenomenon. Further increasing the bond flexibility increasingly destabilizes the crystal relative to the liquid. Thus, it is possible to select a range of bond flexibility where the low and high density liquids are the thermodynamically stable phases, down to rather small temperatures. We refer to this scenario as a "naked", or "crystal-clear" liquid–liquid transition.<sup>46,47</sup>

The coarse-grained NP-DNA model is a perfect candidate for testing these ideas in a more realistic model. Indeed, the model has already a parametric dependence on the width  $\sigma$  of the bonding angle potential.<sup>25</sup> Here we examine how  $\sigma$  (and hence bond orientational flexibility) affects the stability of both the liquid–liquid transition and the competing diamond (DC) and BCC lattice structures. We find that the thermal stability of crystal (measured by the equilibrium melting temperature  $T_m$ ) and of liquid–liquid phase separation (measured by the critical temperature  $T_c$ ) is reduced on increasing  $\sigma$ . However, the effect of changing  $\sigma$  is far more dramatic for  $T_m$  than for  $T_c$ . Consequently, for very narrow bonding angle widths, the LL phase transition is metastable with respect to the crystal, but the LL transition becomes stable with respect to the crystal at a larger bonding width, demonstrating that such a transition is thermodynamically plausible, and not related to any artifacts that might arise due to metastability to a crystal phase. These general findings are similar to those reported in ref. 46, but we emphasize several distinct aspects. First, by examining a model system tethered by DNA-like linkages, we consider a vastly different scale for the range of attraction relative to the core size of the colloidal units. This is also a system that is within the grasp of current experiments. More importantly, the softness of core interactions and the angular variation of bonding interactions introduce an energy gap between low and high density states that is absent in the model of ref. 46. This energy

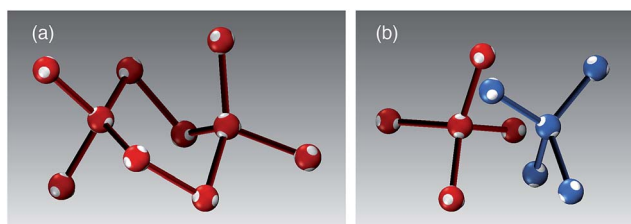


**Fig. 1** Snapshot of molecules in (a) the low-density liquid (LDL) and (b) the high-density liquid (HDL). In each case, we select two nearby NPs which are not directly bonded, and draw the four neighbors to which they are bonded. For LDL, the resulting combined network is fully connected. For HDL, a higher density is achieved by interpenetration of the two locally bonded clusters.

difference plays a vital role in controlling the slope of the liquid–liquid transition, resulting in a phase diagram more like that expected in the case of water.

## 2. Coarse-grained model

We studied the previously proposed effective potential model for particles comprised of four single strands (ss) of DNA tethered to a nanoparticle hub in a tetrahedral orientation.<sup>13,14,27</sup> The effective bonding potential between two ssDNA arms parameterizes the interactions as a function only of the separation of the two nanoparticle cores and of the relative angular orientation, defined by the position of the DNA arms. An additional lock-and-key condition is imposed to mimic the bond selectivity such that each arm combines with only one other ssDNA, effectively imposing the limited valence condition (maximum number of bonded neighbors equal to four). This parameterized potential quantitatively reproduces the structure and phase behavior of the more complex model of NP functionalized with four ssDNA in a tetrahedral orientation.<sup>25</sup> See ref. 25 for a complete description of the effective potential.

The orientational component of the effective potential is defined by the angular distribution  $h_\theta(\theta)$  (where  $\theta$  is the angle between the line connecting the centers of two interacting particles and the direction of the tethered DNA strand), which is described by a Gaussian function, *i.e.*

$$h_\theta(\theta) = \frac{A}{\sqrt{2\pi\sigma^2}} \exp\left[-\frac{\theta^2}{2\sigma^2}\right], \quad (1)$$

where  $A$  is a normalization constant<sup>11</sup> and  $\sigma$  is the standard deviation. Thus, varying  $\sigma$  allows us to vary the bond orientational flexibility. The larger the variance, the wider is the librational motion of the bonded particles. Previous studies<sup>1,11</sup> of the model focused on the single value  $\sigma = 0.052 \text{ rad}^2$ ,  $\approx 1/20$ . Here, we consider a range of values  $1/7 \leq \sigma^2 \leq 1/32$ , where the liquid–liquid transition is accessible on reasonable computational time scales.

We present our results in the reduced units defined by the effective potential.<sup>13,25</sup> In this case, energies (and thus temperature) are determined relative to the binding energy of a single base pair, lengths are in units of base-pair separation within the ssDNA, and the mass is in units of nucleotide mass. Since the model is not intended to be a quantitative representative of the chemical details of DNA, we do not attempt to parameterize the more subtle effects arising from differences in base binding energy (A–T *versus* C–G) or sequence dependent variations.

## 3. Simulation methods

### 3.1. Phase diagram of the amorphous phases

To study the phase diagrams of the amorphous phases, we implement the successive umbrella sampling (SUS) method,<sup>48</sup> which requires that we evaluate the probability distribution  $p_{\mu VT}(N)$  that a system at given temperature  $T$  and chemical potential  $\mu$  in a volume  $V$  contains exactly  $N$  particles. Having obtained a very accurate numerical representation of  $p_{\mu VT}(N)$  (and hence of the density distribution  $p_{\mu VT}(\rho)$ , where  $\rho = N/V$ ) for

a given  $\mu$ , it is possible to evaluate  $p_{\mu' VT}(N)$  for any other  $\mu'$  using the method of histogram reweighting. Formally,

$$p_{\mu' VT}(N) = p_{\mu VT}(N) e^{\beta(\mu' - \mu)N} \frac{\mathfrak{Z}_{\mu' VT}}{\mathfrak{Z}_{\mu VT}} \quad (2)$$

where  $\beta = 1/k_B T$  and  $\mathfrak{Z}_{\mu VT}$  is the grand-canonical partition function. While  $\mathfrak{Z}_{\mu VT}$  is not explicitly known, the necessary ratio is fixed simply by the normalization condition  $\sum_N p_{\mu VT}(N) = 1$ .

Finally, the coexistence between different phases is identified by determining the value of  $\mu'$  for which  $p_{\mu' VT}(N)$  exhibits two distinct peaks with an equal area. The mean density of each of these peaks defines the density of the coexisting phases. To simplify the notation, in the remaining text we will drop the subscript  $\mu VT$  and indicate the probability only by  $p(N)$ .

The challenge of the SUS method is the accurate evaluation of  $p(N)$ . To do so, the range of values  $0 < N < N_{\max}$  under consideration is divided into  $N_{\max}$  overlapping intervals  $i$  such that  $N \in [N_i, N_i + 1]$ . In each window a ‘restricted’ grand-canonical Monte-Carlo (GCMC) simulation is performed, rejecting moves that would insert or delete a particle outside the range. From each simulation, one calculates how often a state with  $N_i$  particles is visited relative to the state with  $N_i + 1$ , providing the probability ratio  $p(N_i)/p(N_i + 1)$ . By combining the data in the overlapping windows from the  $N_{\max}$  simulations and enforcing normalization, the complete probability distribution  $p(N)$  is constructed.

The advantages of using this method are the possibility to sample all microstates without any biasing function and the relative simplicity to parallelize the run, with the speed gain scaling linearly with the number of processors. For the specific system we study, we use a cubic box of length  $L = 55$ , and the  $\mu$  value varies with  $T$ ; the specific value of  $\mu$  is usually not critical, since histogram reweighting is used to reconstruct the  $p(N)$  data for a broad range of  $\mu$  values. To sample the range of densities relevant to the liquid–gas and liquid–liquid transition for the chosen  $L$ , we perform restricted GCMC simulations with  $N \in [N_i, N_i + 1]$  over the range  $N_i = 0$  to  $N_i = 299$  molecules for each temperature studied. In other words, for each  $T$  and  $\sigma$  we consider, we perform 300 simulations with overlapping intervals of one bin. Considering the number of temperatures and  $\sigma$  values studied, we present results from around twenty thousand individual simulations; fortunately modest cluster computing facilities make this task manageable. Note that, in general, the method can also be extended to enable reweighting to different  $T$  values, provided that the combined probability  $p(N, E)$  (where  $E$  is the energy) is adequately sampled.

The knowledge of  $p(N)$  from  $N = 0$  onward makes it possible also to evaluate the equation of state of the model (parametric in  $\mu$ ), *via* the relation for the pressure<sup>49</sup>

$$P(T, V) = -\frac{k_B T}{V} \ln p(0) \quad (3)$$

combined with

$$\rho(T, V) = \sum_N N p(N) / V \quad (4)$$

where  $p(0)$  is the probability for  $N = 0$  molecules at a given  $(\mu, V, T)$ , which is obtained from the histogram reweighted data.

To provide a clearer picture of the process by which our data are obtained, we show an example of  $p(N)$  for bonding width  $\sigma^2 = 1/16$ , at  $T = 0.0910$  and  $\mu/kT = -13.2$  in Fig. 2(a), which is below the critical temperature for both liquid–gas and liquid–liquid phase separation. The SUS method enables us to obtain data for  $p(N)$  that effectively samples an enormous range of probabilities, here spanning 50 orders of magnitude. It is this extreme accuracy that allows for reweighting  $p(N)$  to a broad range of  $\mu$  values, including at coexistence, as shown in Fig. 2(b). We identify the  $\mu$  value for coexistence of the phases by finding the reweighting that yields two distinct peaks of equal areas. Accordingly, we can evaluate the mean densities of these coexisting phases, which generates the  $T$ – $\rho$  phase diagram.

### 3.2. Melting loci of crystal phases

In addition to the disordered phases, it is important to identify the equilibrium melting loci of the relevant open crystals, diamond and BCC. We calculate the melting temperature of crystal phases using the ‘interface’ method, in which a crystal is placed

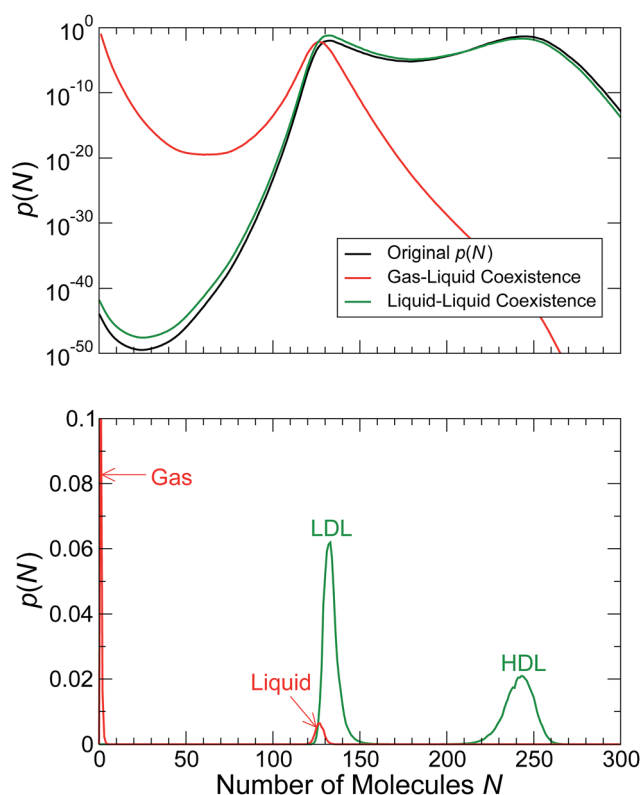


Fig. 2 (a) Example of the distribution  $p(N)$  of molecular occupancy for  $\sigma^2 = 1/16$ , at  $T = 0.0910$  and  $\mu/kT = -13.2$ , on a logarithmic scale (black line). Note that the scale of  $p(N)$  covers 50 orders of magnitude, enabling reweighting over a large range of  $\mu$ . The data are reweighted according to eqn (2) to generate  $p(N)$  for the liquid–gas (red) and liquid–liquid (green) coexistences. (b) The distributions  $p(N)$  for the liquid–gas and liquid–liquid coexistence on a linear scale to more readily identify the two coexisting phases.

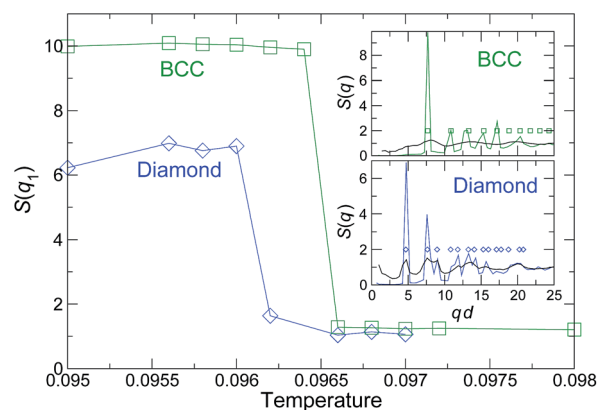


Fig. 3 Example of the identification of the melting temperature  $T_m$  for the diamond and BCC lattices for  $\sigma = 1/32$ . The amplitude of the primary peak  $q_1$  of the structure factor  $S(q_1)$  has an essentially discontinuous drop upon melting of the crystal, allowing us to narrow the range for  $T_m$ . The insets show the full structure factors  $S(q)$  from which the first peak is extracted. For each crystal, we show  $S(q)$  immediately below (green or blue) and above (in black)  $T_m$ . The small symbols in the insets mark the expected Bragg peak locations for ideal diamond or BCC organizations. We obtain similar data for all other  $\sigma$  studied.

in contact with the fluid at a fixed temperature and pressure (see Section 8.1.4 of ref. 50). In this case, we place an ideal diamond or a BCC crystal in contact with an amorphous fluid phase with similar density. The crystal region consists of 512 molecules for the case of the diamond lattice, and 432 molecules for the BCC lattice; the corresponding number of molecules are used in the fluid phase, resulting in a simulation cell that is roughly twice as long in the direction normal to the fluid–crystal interface. Box dimensions parallel and perpendicular to the interface vary independently to relax any potential stress on the crystal phase. The interface in this case is unstable, so that the system will progress toward either an entirely crystal or an entirely fluid state.

We identify melting by the disappearance of the Bragg peaks in  $S(q)$ , as illustrated by Fig. 3 at one example pressure for both the diamond and BCC systems. Note that the connectivity of the BCC crystal in this case is that of two distinct, interpenetrating diamond lattices. To map out the melting loci  $T_m$  in the region of interest, we study many  $P$  for each  $T$ . Our results for the precise location of  $T_m$  are limited to  $T > 0.090$ . For lower  $T$  the kinetics of the crystal–fluid interface become too slow for a precise estimate. In these cases, we are able to place upper bounds on  $T_m$  by the lowest  $T$  at which melting is clearly observed.

## 4. Results and discussion

We now examine how changing the bond orientational flexibility ( $\sigma^2$ ) of the potential affects the liquid–liquid phase transition and its stability relative to the crystal phases.

Fig. 4 shows the phase diagram of the three amorphous phases – gas, low-density liquid (LDL), and high-density liquid (HDL) – as well as the diamond and BCC crystals in the  $T$ – $\rho$  plane for six values of the variance  $\sigma^2$  of the angular potential.

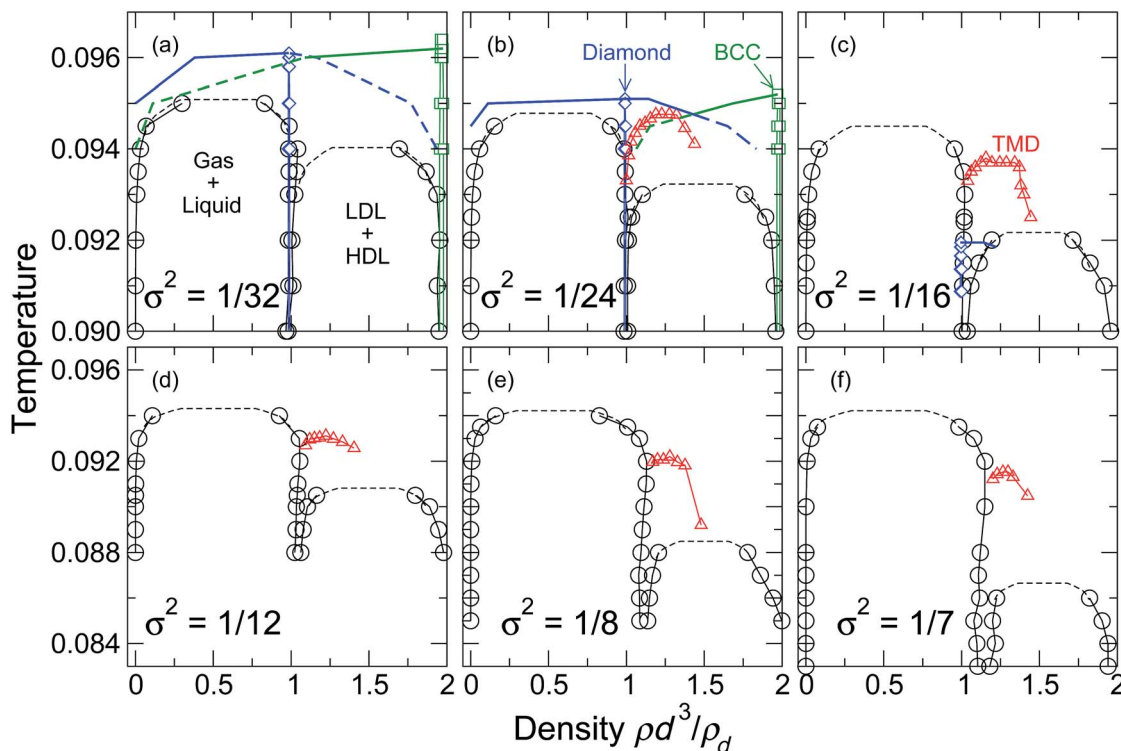


Fig. 4  $T$ - $\rho$  phase diagram for various bond orientational flexibility values  $\sigma^2$ . The density is scaled by the bonding distance  $d^3$  to facilitate comparison with the diamond lattice  $\rho_d$ . The black circles indicate the bounds of the phase coexistence of the amorphous phases (gas, LDL, and HDL). The dotted black lines estimate the upper bound of the coexistence region. The blue diamonds bound the thermodynamically stable, single-phase region for the diamond lattice ( $\rho d^3/\rho_d = 1$ ), and the green squares indicate the stability region of the BCC lattice ( $\rho d^3/\rho_d = 2$ ). These regions are extremely narrow in density, so that they appear as nearly vertical lines in this representation. The blue (diamond lattice) and green (BCC lattice) lines indicate the crystal–fluid coexistence boundaries; the lines are solid for the coexistence with a stable crystal, and dashed for the coexistence with a metastable crystal. Thus, in panels (a) and (b), the combined solid blue and green lines indicate the region where a crystal is in the thermodynamically stable state. The red triangles indicate the locus of temperature of maximum density (TMD) of the amorphous phase.

For convenience, we plot density  $\rho = N/V$  scaled by the most probable separation  $d$  of a bonded neighbor and the density  $\rho_d$  for a diamond lattice with unit lattice spacing. Using this scaling,  $\rho d^3/\rho_d = 1$  corresponds to the density for a diamond (cubic or hexagonal) lattice; similarly,  $\rho d^3/\rho_d = 2$  corresponds to BCC density (two interpenetrating diamond lattices).

For all  $\sigma^2$  values shown, we observe a liquid–liquid transition, in addition to the standard gas–liquid transition. For the liquid–gas transition,  $T_c$  is essentially independent of  $\sigma^2$  and the liquid phase coexisting with the gas has always a density approaching  $\rho d^3/\rho_d \approx 1$ , indicating the predominance of local tetrahedral order. In contrast, the  $T_c$  of the liquid–liquid transition decreases with  $\sigma^2$ , suggesting that bond directionality favors the liquid–liquid phase separation. This second phase transition involves a locally tetrahedral low-density ( $\rho d^3/\rho_d \approx 1$ ) and an interpenetrating high-density phase ( $\rho d^3/\rho_d \approx 2$ ). The  $\sigma$  value previously discussed in ref. 1 is intermediate to the  $\sigma^2 = 1/16$  and  $1/24$  cases.

Like  $T_c$  for the LL critical point, the  $T_m$  of crystal phases is also very sensitive to  $\sigma^2$ . The highest  $T$  at which the crystals are thermodynamically stable quickly drops with increasing  $\sigma^2$ , confirming the previous finding<sup>40,42</sup> that the stability of the crystals is strongly affected by bond flexibility. This can be understood from the fact that larger flexibility allows a large

variety of fully bonded states that are disordered. These disordered states will have nearly the same energy as the ordered state, but larger entropy, and hence lower free energy.

It is interesting to observe that, for highly directional bonds ( $\sigma^2 \leq 1/24$ ), the crystal states are so strongly favored that the upper bound of melting for both DC and BCC lattices exceeds the critical temperature of even the gas–liquid transition. Consequently, both the gas–liquid and liquid–liquid transitions are metastable with respect to the crystal (Fig. 4(a and b)). For these very directed, inflexible linkages, the thermodynamically stable phase diagram consists of only crystal phases and a super-critical fluid. On increasing flexibility, the destabilization of the crystal results in the gas–liquid transition becoming thermodynamically stable. This is reminiscent of the appearance of the gas–liquid transition as a stable phase in isotropic colloids, when the range of interaction increases beyond  $\approx 25\%$  of the particle size,<sup>51,52</sup> a phenomenon confirmed also for directional interactions.<sup>53,54</sup> In this respect, large bond flexibility acts as an effectively increased interaction range.

Both the liquid–liquid transition and the crystallization transition are thus significantly affected by bond flexibility. Still, the rate at which the two phenomena is sensitive to  $\sigma^2$  appears to be different. As a consequence, for  $\sigma^2 \geq 1/16$ , the LL critical point becomes thermodynamically stable with respect to the

crystal. For  $\sigma^2 \geq 1/12$ , the crystallization kinetics become extremely slow, preventing us from accurately determining the complete crystal melting locus. However, in all cases we confirm (again using the interface method) that both diamond and BCC crystals melt at  $P_c$  for  $T$  significantly below  $T_c$  for the liquid–liquid critical point, so that the stability of the LL critical point is assured.

To better grasp the competition between the crystal phases and the LL transition, as well as to understand the relationship to the anomalies of water-like systems, we construct the  $T$ – $P$  representation of the phase diagram. Fig. 5 shows the resulting  $T$ – $P$  diagram for the same  $\sigma^2$  values shown in the  $T$ – $\rho$  diagrams. The relative crystal stabilities and the crossover from metastability to stability of the LL transition are best illustrated by Fig. 6, which shows the  $T_c$  of the LL transition and  $T_m$  of the diamond and BCC crystals at the critical pressure  $P_c$  for the LL transition, as bond flexibility  $\sigma$  is increased. The graph indicates, along a thermodynamic isobaric path at  $P_c$ , the sequence of phenomena (LL critical point or DC or BCC crystallization) that are encountered on cooling. For very rigid bonds, the BCC has a larger  $T_m$  at  $P_c$  and hence it is a more stable phase.

However, since  $T_m$  for the BCC lattice decreases more rapidly with increasing  $\sigma$  than for the diamond lattice, the diamond lattice becomes a more stable crystal at  $P_c$  for  $\sigma^2 > 1/24$ . Finally, at  $\sigma^2 \approx 1/16$  the liquid–liquid critical point bulges out and becomes thermodynamically accessible from the liquid side. On further increasing  $\sigma^2$  BCC and DC melting  $T$  decreases so quickly that the LL remains the only accessible thermodynamic phenomenon, so that crystallization cannot interfere with the “crystal clear” liquid–liquid transition.

The  $T$ – $P$  representation is also helpful to quantify water-like anomalies. In particular, Fig. 5 shows the line of isobaric density maxima, or temperature of maximum density (TMD), for the model at each  $\sigma^2$  considered. We observe that the locus of density maxima ‘retrace’ with pressure. The same curves are also shown for completeness in the  $T$ – $\rho$  plane in Fig. 4. In the case of water, the possible presence of a liquid–liquid transition is likely intimately connected with the many anomalous properties of water. In particular, the presence of the density anomaly in water demands that entropy and volume changes are negatively correlated; in the context of the Clausius–Clapeyron relation, this usually leads to coexistence lines in the

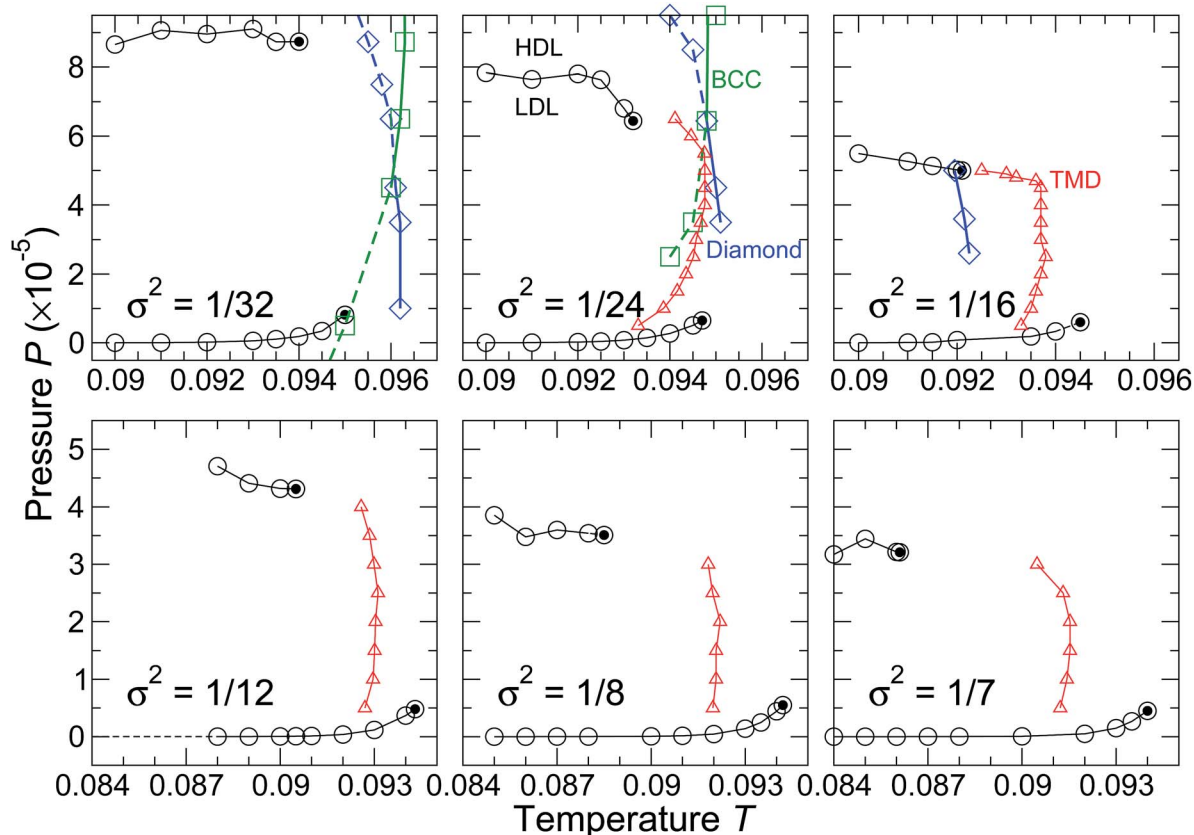


Fig. 5  $T$ – $P$  phase diagram for various bond orientational flexibility values  $\sigma^2$ . For  $\sigma^2 < 1/16$ , the liquid–liquid transition is metastable with respect to the crystals. The melting locus for the diamond lattice is shown by the blue diamonds and for BCC by the green squares. The solid lines interpolate between points, and indicate melting of a stable crystal. The dashed lines indicate melting of the crystal, where the melting is metastable to another crystal. For  $\sigma^2 > 1/16$ , we cannot accurately evaluate the melting locus, but confirm that crystals melt well below  $T_c$  at  $P_c$  for the LL transition. Also note that the LL coexistence line generally has a negative slope, a feature expected for water, but not present in many simple models exhibiting a liquid–liquid transition. The red triangles indicate the locus of temperature of maximum density (TMD) of the amorphous phase.

anomalous region of the  $T$ - $P$  plane that are negatively sloped (strictly speaking, a negatively sloped coexistence line can exist without a density anomaly). For example, the liquid-ice  $I_h$  melting line is negatively sloped just below the TMD, in contrast to normal liquids. Similarly, the LDL-HDL coexistence line, if it does exist in water, is also expected to be negatively sloped. Curiously, many simple, spherically symmetric models that exhibit a liquid-liquid transition do not share the negative slope in  $T$ - $P$  of the LDL-HDL line. In contrast, the present model does exhibit negatively sloped LDL-HDL and diamond-liquid coexistence lines. A positive slope was also observed in the modified tetrahedral patch Kern-Frenkel model – which also exhibits a stable LL transition.<sup>46</sup> An important difference between that model and the one we study is that the energy for all bonded orientations is identical for the patchy particle model, while here there is an energy penalty as the orientation deviates from the preferred direction, as well as when particles change their relative distance. Consequently, in the patchy model, the energy of the two fully bonded networks (BCC) is identical to a single network (DC). Consideration of the energy cost of interpenetration, either due to the orientational dependence of the bonding energy<sup>55</sup> or due to the generic repulsive contribution, may be an important feature to reproduce a negatively sloped LDL-HDL transition line in the phase diagram.

To clarify the energetic origin of the LL transition, we investigate the density dependence of the potential energy for  $T$  close to  $T_c$ . Fig. 7 shows the potential energy for three  $\sigma$  values at temperatures above, at, and below the  $T_c$  for liquid-liquid phase separation. The data, originating from the SUS simulations, cover the entire range of densities, from the gas phase to the high-density liquid phase, including the coexistence regions. The energy in the unstable region of density depends on the extent of the interface between gas and liquid or between the LDL and HDL phases, and is reported here only for

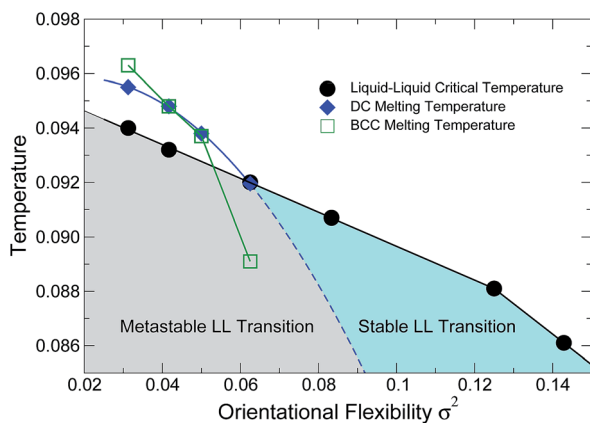


Fig. 6 Relative stability of crystal and amorphous states as a function of bond orientational flexibility. As the variance  $\sigma^2$  for the bond angle potential grows,  $T_c$  and  $T_m$  (evaluated at  $P_c$ ) decrease. However, the  $T_m$  for crystals decreases significantly more rapidly than  $T_c$  of the LL transition, opening a window in the phase diagram (shaded aqua) where thermodynamically stable liquid-liquid coexistence occurs without the intervention of crystallization.

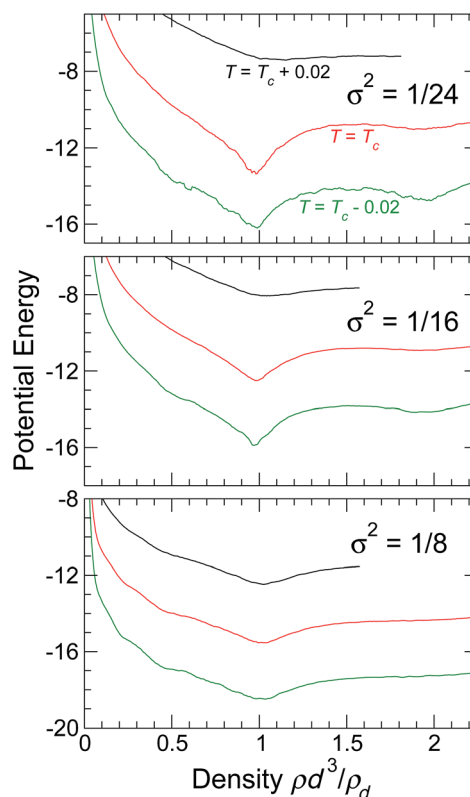


Fig. 7 Potential energy as a function of density for (a)  $\sigma^2 = 1/24$ , (b)  $\sigma^2 = 1/16$ , and (c)  $\sigma^2 = 1/8$ . For each bond flexibility, we show three temperatures near  $T_c$  for the liquid-liquid phase separation.

completeness. For relatively stiff bonds ( $\sigma^2 = 1/24$ ), minima in the potential energy are apparent near  $\rho d^3/\rho_d \approx 1$  and  $\rho d^3/\rho_d \approx 2$ , which are better resolved on cooling. For all  $\sigma$ , the depth energy minimum of the single networked phase (low density,  $\rho d^3/\rho_d \approx 1$ ) is noticeably greater than that of the high-density phase. However, as bonds become more flexible (increasing  $\sigma$ ), the energy minimum for the high-density phase becomes difficult to distinguish. The presence of two minima in the density dependence of the potential energy expresses the strong coupling between local density and bonding induced by the directionality of the interaction. When the average distance between the particles coincides with the possibility of forming one full network (the so-called optimal density) or two interpenetrating networks, then the energy is low. When the average distance between the particles does not match the network values, then – in order to maximize the number of bonds – the system prefers to separate into two phases with optimal network densities.

To put our findings in the context of other tetrahedrally coordinated fluids, we examine how the order of our system varies as we change the bonding flexibility. More specifically, ref. 56 found that the data for a broad range of tetrahedral fluids can be organized around the parametric variation of the “pre-peak” in the structure factor  $S(q)$  relative to the angle  $\phi$  defined by the connection between three bonded neighbors. Accordingly, in Fig. 8 we show  $S(q)$  and the distribution  $P(\phi)$  for various  $\sigma^2$  at the ideal density  $\rho d^3/\rho_d = 1$ ; data are shown at the critical

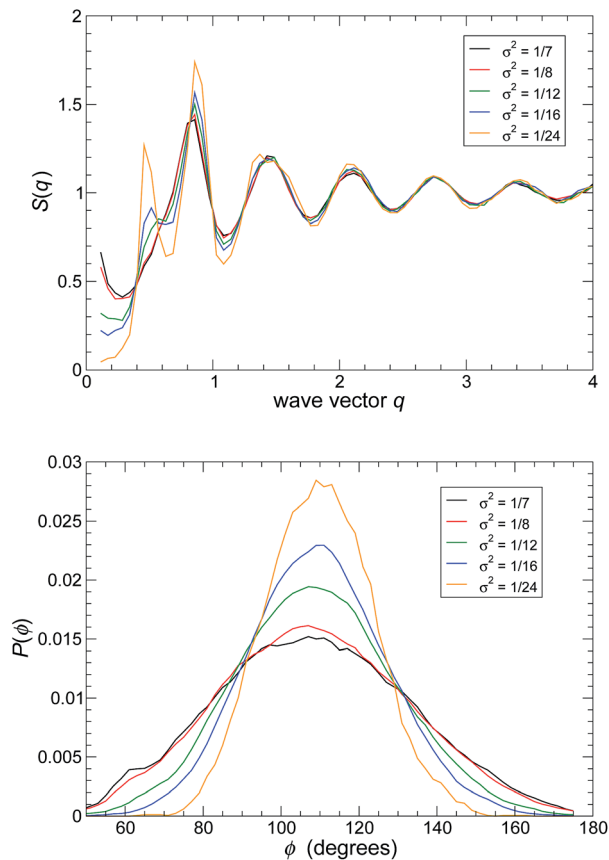


Fig. 8 Structure of the fluid at the critical temperature  $T_c$  for LL phase separation at the ideal tetrahedral density  $\rho d^3/\rho_d = 1$ , quantified by (a) the structure factor  $S(q)$  and (b) the distribution  $P(\phi)$  of the angle  $\phi$  defined by three bonded neighbors.

temperature  $T_c(\sigma)$  to simplify comparison. For rigid bonds (small  $\sigma^2$ ),  $S(q)$  displays a prominent pre-peak at  $q_1 \approx 0.5$ , indicative of the tetrahedral organization. As the bond flexibility

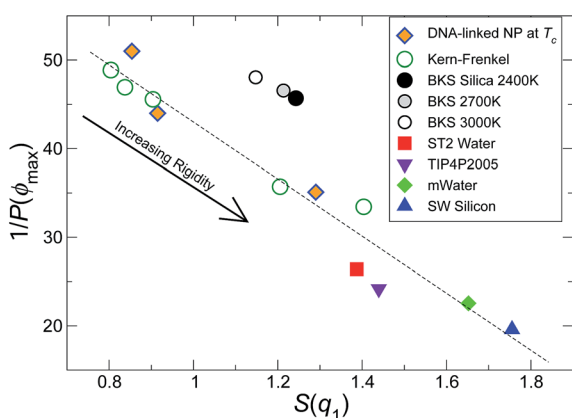


Fig. 9 Universal description of the structure of tetrahedral fluids, given by the variation of the pre-peak  $S(q_1)$  with the inverse of the peak in  $P(\phi_{\max})$ . Data for the present study are shown by orange diamonds, at  $\rho d^3/\rho_d = 1$  and  $T_c$  for LL phase separation. From left to right, the  $\sigma^2$  values for these points are 1/12, 1/16, and 1/24. The data for the other systems were taken from ref. 56.

increases, this pre-peak shrinks, and the pre-peak is not readily identifiable for  $\sigma^2 > 1/12$ , indicating the growing distortion of the network. Correspondingly, the angle distribution  $P(\phi)$  broadens as the bond flexibility increases, and the amplitude  $P(\phi_{\max})$  of the peak location  $\phi_{\max}$  decreases. These changes are not independent, and we see the explicit relation in Fig. 9, where we plot the amplitude of the pre-peak  $S(q_1)$  as a function of  $1/P(\phi_{\max})$ , along with data for a collection of other tetrahedral fluids. These data demonstrate the underlying similarity of these fluids. Moreover, this provides some guidance as to in which cases we might expect a possible stable liquid–liquid transition. Specifically, using the fact that the LL transition is thermodynamically stable for  $\sigma^2 \geq 1/8$ , we expect that for  $S(q_1) \leq 0.9$  and  $P(\phi_{\max}) \leq 0.02$  (at  $T_c$  and the diamond density  $\rho d^3/\rho_d = 1$ ), the LL transition will be stable relative to the crystal.

## 5. Conclusions

We have investigated the interplay between crystallization and the liquid–liquid transition in a model for limited valence particles composed of four single-stranded DNA grafted on a central core in a tetrahedral arrangement. We have tuned the orientational flexibility of the bonds to investigate its role on both the liquid–liquid transition and crystal formation. Consistent with predictions based on primitive models of tetrahedrally coordinated particles,<sup>40,42</sup> we have found that bond directionality controls the thermodynamic stability of the crystal. On increasing flexibility, the melting temperature decreases, stabilizing the liquid state. As a result, the liquid–liquid transition emerges from metastability. Under these conditions, the critical point and the phase separation process becomes “crystal clear”<sup>47</sup> and can be approached without the fear of originating crystal seeds. Our work thus shows that, when there is no stable crystal, the liquid–liquid transition can not be mistaken as a failed crystallization.<sup>32</sup>

Our results provide further evidence that, for tetrahedrally coordinated particles, the liquid–liquid transition is a genuine phenomenon, even if commonly hidden by crystallization. This observation holds not only for colloidal tetrahedral particles but apparently also for their atomic and molecular counterparts, including water, silica, silicon, and carbon to name a few. The delicate interplay of softness (controlling the ability to interpenetrate) and bond directionality dictate the relative distance between the melting and the critical point, and hence the possibility to approach the liquid–liquid critical point without the interference of crystallization. The present study confirms<sup>46</sup> that systems with highly directional bonds (as in silicon and water<sup>56</sup>) are prone to crystallization. Our findings suggest that in such a case, a liquid–liquid critical point is present, but hidden in the metastable region. While the metastable region is sometimes accessible to careful experiments, rapid crystallization typically makes much of this region practically inaccessible – and thus often termed “no-man’s land”. Even if the critical point cannot be accessed experimentally, its presence affects large regions of temperatures and pressures where the liquid state is stable.<sup>28,29,57</sup>

Finally, our results provide a possible route to experimentally design a colloidal system to mimic water-like behavior. Micron-size colloidal particles with specific directionality have been recently synthesized<sup>58</sup> and offer an alternative to DNA-grafted nanoparticles or DNA nano-constructs.<sup>59</sup> A colloidal model for water where the width of the no-man's land can be controlled and the liquid-liquid transition can be exposed is hopefully soon within reach.

## Acknowledgements

We thank S. Sastry and F. Smallenburg for helpful discussions. We acknowledge support from ERC-226207-PATCH-YCOLLOIDS, MIUR PRIN, and from Wesleyan University for computing resources.

## References

- 1 C. W. Hsu, J. Largo, F. Sciortino and F. W. Starr, *Proc. Natl. Acad. Sci. U. S. A.*, 2008, **105**, 13711.
- 2 P. Poole, F. Sciortino, U. Essmann and H. Stanley, *Nature*, 1992, **360**, 324.
- 3 P. H. Poole, T. Grande, C. A. Angell and P. F. McMillan, *Science*, 1997, **275**, 322.
- 4 S. Sastry and C. A. Angell, *Nat. Mater.*, 2003, **2**, 739.
- 5 I. Saika-Voivod, F. Sciortino and P. Poole, *Phys. Rev. E: Stat. Phys., Plasmas, Fluids, Relat. Interdiscip. Top.*, 2000, **63**, 011202.
- 6 Y. Katayama, T. Mizutani, W. Utsumi, O. Shimomura, M. Yamakata and K.-I. Funakoshi, *Nature*, 2000, **403**, 170.
- 7 A. Cadien, Q. Y. Hu, Y. Meng, Y. Q. Cheng, M. W. Chen, J. F. Shu, H. K. Mao and H. W. Sheng, *Phys. Rev. Lett.*, 2013, **110**, 125503, DOI: 10.1103/PhysRevLett.110.125503.
- 8 E. A. Jagla, *J. Chem. Phys.*, 1999, **111**, 8980, <http://scitation.aip.org/content/aip/journal/jcp/111/19/10.1063/1.480241>.
- 9 A. Skibinsky, S. V. Buldyrev, G. Franzese, G. Malescio and H. E. Stanley, *Phys. Rev. E: Stat., Nonlinear, Soft Matter Phys.*, 2004, **69**, 061206, DOI: 10.1103/PhysRevE.69.061206.
- 10 C. W. Hsu and F. W. Starr, *Phys. Rev. E: Stat., Nonlinear, Soft Matter Phys.*, 2009, **79**, 041502.
- 11 W. Dai, C. W. Hsu, F. Sciortino and F. W. Starr, *Langmuir*, 2010, **26**, 3601.
- 12 E. Zaccarelli, F. Sciortino and P. Tartaglia, *J. Chem. Phys.*, 2007, **127**, 174501, <http://scitation.aip.org/content/aip/journal/jcp/127/17/10.1063/1.2799522>.
- 13 F. W. Starr and F. Sciortino, *J. Phys.: Condens. Matter*, 2006, **18**, L347, <http://stacks.iop.org/0953-8984/18/L347>.
- 14 J. Largo, F. W. Starr and F. Sciortino, *Langmuir*, 2006, **23**, 5896.
- 15 S. C. Glotzer and M. J. Solomon, *Nat. Mater.*, 2007, **6**, 557.
- 16 A. B. Pawar and I. Kretschmar, *Macromol. Rapid Commun.*, 2010, **31**, 150, DOI: 10.1002/marc.200900614.
- 17 E. Zaccarelli, I. Voivod, S. Buldyrev, A. Moreno, P. Tartaglia and F. Sciortino, *J. Chem. Phys.*, 2006, **124**, 124908.
- 18 E. Bianchi, J. Largo, P. Tartaglia, E. Zaccarelli and F. Sciortino, *Phys. Rev. Lett.*, 2006, **97**, 168301.
- 19 F. Sciortino, A. Giacometti and G. Pastore, *Phys. Rev. Lett.*, 2009, **103**, 237801.
- 20 D. J. Kraft, R. Ni, F. Smallenburg, M. Hermes, K. Yoon, D. A. Weitz, A. van Blaaderen, J. Groenewold, M. Dijkstra and W. K. Kegel, *Proc. Natl. Acad. Sci. U. S. A.*, 2012, **109**, 10787.
- 21 N. C. Seeman, *J. Theor. Biol.*, 1982, **99**, 237.
- 22 N. C. Seeman, *Nature*, 2003, **421**, 427.
- 23 C. A. Mirkin, R. L. Letsinger, R. C. Mucic and J. J. Storhoff, *Nature*, 1996, **382**, 607.
- 24 A. P. Alivisatos, K. P. Johnsson, X. Peng, T. E. Wilson, C. J. Loweth, M. P. Bruchez and P. G. Schultz, *Nature*, 1996, **382**, 609.
- 25 J. Largo, P. Tartaglia and F. Sciortino, *Phys. Rev. E: Stat., Nonlinear, Soft Matter Phys.*, 2007, **76**, 011402.
- 26 T. E. Ouldridge, I. G. Johnston, A. A. Louis and J. P. K. Doye, *J. Chem. Phys.*, 2009, **130**, 065101, pages 11.
- 27 P. E. Theodorakis, C. Dellago and G. Kahl, *J. Chem. Phys.*, 2013, **138**, 025101, <http://scitation.aip.org/content/aip/journal/jcp/138/2/10.1063/1.4773920>.
- 28 O. Mishima and H. E. Stanley, *Nature*, 1998, **396**, 329.
- 29 P. G. Debenedetti, *J. Phys.: Condens. Matter*, 2003, **15**, R1669.
- 30 P. Poole, F. Sciortino, T. Grande, H. Stanley and C. Angell, *Phys. Rev. Lett.*, 1994, **73**, 1632.
- 31 M. Yamada, S. Mossa, H. E. Stanley and F. Sciortino, *Phys. Rev. Lett.*, 2002, **88**, 195701, DOI: 10.1103/PhysRevLett.88.195701.
- 32 D. T. Limmer and D. Chandler, *J. Chem. Phys.*, 2011, **135**, 134503.
- 33 F. Sciortino, I. Saika-Voivod and P. H. Poole, *Phys. Chem. Chem. Phys.*, 2011, **13**, 19759.
- 34 Y. Liu, J. C. Palmer, A. Z. Panagiotopoulos and P. G. Debenedetti, *J. Chem. Phys.*, 2012, **137**, 214505.
- 35 P. H. Poole, R. K. Bowles, I. Saika-Voivod and F. Sciortino, *J. Chem. Phys.*, 2013, **138**, 034505.
- 36 J. L. Abascal and C. Vega, *J. Chem. Phys.*, 2010, **133**, 234502.
- 37 T. A. Kesselring, G. Franzese, S. V. Buldyrev, H. J. Herrmann and H. E. Stanley, *Sci. Rep.*, 2012, **2**, 474.
- 38 J. C. Palmer, F. Martelli, Y. Liu, R. Car, A. Z. Panagiotopoulos and P. G. Debenedetti, *Nature*, 2014, **510**, 385, DOI: 10.1038/nature13405, ISSN 0028-0836.
- 39 M. Maldovan and E. L. Thomas, *Nat. Mater.*, 2004, **3**, 593, DOI: 10.1038/nmat1201.
- 40 F. Romano, E. Sanz and F. Sciortino, *J. Chem. Phys.*, 2011, **134**, 174502, pages 8.
- 41 E. G. Noya, C. Vega, J. P. K. Doye and A. A. Louis, *J. Chem. Phys.*, 2010, **132**, 234511, <http://scitation.aip.org/content/aip/journal/jcp/132/23/10.1063/1.3454907>.
- 42 F. Smallenburg and F. Sciortino, *Nat. Phys.*, 2013, **9**, 554.
- 43 F. J. Martinez-Veracoechea, B. M. Mladek, A. V. Tkachenko and D. Frenkel, *Phys. Rev. Lett.*, 2011, **107**, 045902.
- 44 S. Whitlam, I. Tamblyn, T. K. Haxton, M. B. Wieland, N. R. Champness, J. P. Garrahan and P. H. Beton, *Phys. Rev. X*, 2014, **4**, 011044, DOI: 10.1103/PhysRevX.4.011044.
- 45 L. Rovigatti, F. Smallenburg, F. Romano and F. Sciortino, *ACS Nano*, 2014, **8**, 3567, DOI: 10.1021/nn501138w.

- 46 F. Smallenburg, L. Filion and F. Sciortino, *Nat. Phys.*, 2014, **10**, 653, DOI: 10.1038/nphys3030, ISSN 1745-2481.
- 47 F. W. Starr, *Nat. Phys.*, 2014, **10**, 628, DOI: 10.1038/nphys3059, ISSN 1745-2481.
- 48 P. Virnau and M. Müller, *J. Chem. Phys.*, 2004, **120**, 10925.
- 49 T. Vissers, Z. Preisler, F. Smallenburg, M. Dijkstra and F. Sciortino, *J. Chem. Phys.*, 2013, **138**, 164505.
- 50 C. Vega, E. Sanz, J. Abascal and E. Noya, *J. Phys.: Condens. Matter*, 2008, **20**, 153101.
- 51 V. J. Anderson and H. N. W. Lekkerkerker, *Nature*, 2002, **416**, 811.
- 52 C. F. Tejero, A. Daanoun, H. N. W. Lekkerkerker and M. Baus, *Phys. Rev. Lett.*, 1994, **73**, 752, DOI: 10.1103/PhysRevLett.73.752.
- 53 F. Romano, E. Sanz and F. Sciortino, *J. Phys. Chem. B*, 2009, **113**, 15133.
- 54 F. Romano, E. Sanz and F. Sciortino, *J. Chem. Phys.*, 2010, **132**, 184501.
- 55 Y. Tu, S. V. Buldyrev, Z. Liu, H. Fang and H. E. Stanley, *Europhys. Lett.*, 2012, **97**, 56005, <http://stacks.iop.org/0295-5075/97/i=5/a=56005>.
- 56 I. Saika-Voivod, F. Smallenburg and F. Sciortino, *J. Chem. Phys.*, 2013, **139**, 234901.
- 57 V. Holten, C. E. Bertrand, M. A. Anisimov and J. V. Sengers, *J. Chem. Phys.*, 2012, **136**, 094507.
- 58 Z. Wang and C. Holm, *Phys. Rev. E: Stat., Nonlinear, Soft Matter Phys.*, 2003, **68**, 041401.
- 59 S. Biffi, R. Cerbino, F. Bomboi, E. M. Paraboschi, R. Asselta, F. Sciortino and T. Bellini, *Proc. Natl. Acad. Sci. U. S. A.*, 2013, **110**, 15633.